Geophysical and Astrophysical Fluid Dynamics,
Vol. 100, Nos. 4–5, August–October 2006, 319–339

Taylor & Francis
Taylor & Francis Group

Azimuthal winds, convection and dynamo action in the polar regions of planetary cores

BINOD SREENIVASAN† and CHRIS A. JONES*‡

†School of Earth and Environment, University of Leeds, Leeds LS2 9JT, UK
‡Department of Applied Mathematics, University of Leeds, Leeds LS2 9JT, UK

(*Received 12 December 2005; in final form 12 May 2006*)

We investigate azimuthal winds in planetary cores using a thermal convection-driven dynamo. When inertial forces are not negligible in the equation of motion, the inertially driven thermal winds are cyclonic. When the Lorentz forces are strong enough, we find anticyclonic thermal winds as observed in the Earth's polar region from secular variation data. Under strong thermal convection, the azimuthal flow is created by the magnetic mode with one or more coherent, strong upwellings inside the tangent cylinder (TC), offset from the polar axis. We also find that, as the convection in the TC becomes stronger, these vortex plumes shrink in size, consistent with the convection being controlled by the magnetic field. In addition, strong upwellings in the TC could expel magnetic field in its path, creating regions of weak or even reverse flux patches. These patches drift westward, but at a significantly slower angular speed than the rotation about the vortex itself. Calculations with electrically conducting and stress-free boundaries reveal that the mechanism of generation of polar thermal winds is fairly independent of the boundary conditions imposed, provided the Rayleigh number is high enough to excite the magnetic mode.

Keywords: Polar vortex; Earth's core; Convection; Tangent cylinder; Magnetic mode

1. Introduction

The rapid rotation of the Earth's core divides convection naturally into two distinct regions, inside and outside the tangent cylinder (TC). The TC is an imaginary cylinder which touches the solid inner core and has radius 1220 km, about 0.35 times the radius of the whole fluid core. The TC cuts the core-mantle boundary (CMB) at approximately latitude 70°. Outside the TC the convection occurs much more readily than inside the TC, because the heat and composition there can be convected outward by rolls in which fluid motion is almost independent of the co-ordinate parallel to the rotation axis z, in a mainly geostrophic balance of Coriolis and pressure forces, though the sloping CMB prevents complete geostrophy. Inside the TC, in the polar regions, the heat and composition flux have a substantial component in the z-direction, so the motion

*Corresponding author. Email: cajones@maths.leeds.ac.uk

Geophysical and Astrophysical Fluid Dynamics
ISSN 0309-1929 print/ISSN 1029-0419 online
http://www.tandf.co.uk/journals
DOI: 10.1080/03091920600807864

cannot be independent of z. The buoyancy force has to break the Proudman–Taylor constraint directly, and so the local critical Rayleigh number (Busse 1970) is typically 10 times larger inside the TC than outside it. When non-magnetic convection inside the TC does onset, it has the structure of tall thin columns (Chandrasekhar 1961) so that the bulk viscosity can also help overcome the Proudman–Taylor constraint. The preferred mode of convection inside the tangent cylinder will be rising and falling plumes with z-vorticity of opposite sign at the top and bottom of each plume. This is a different structure from the rolls outside the tangent cylinder which have fairly constant z-vorticity in each roll, but with z-velocity changing sign as the roll crosses the equatorial plane.

Because convection inside the TC is much more constrained by the Proudman–Taylor theorem, a magnetic field can have a much stronger effect in breaking that constraint. Outside the TC, the main dynamical effect of the magnetic field is to thicken the convection rolls (Jones *et al.* 2003) and to enhance the flow up and down the rolls (Kageyama and Sato 1997). Inside the tangent cylinder, convection in a rotating magnetic layer onsets either as narrow viscous columns or large-scale magnetic modes that will fill a large fraction of the entire polar region (Chandrasekhar 1961). The Rayleigh number in the core is large enough to ensure that convection is occurring in the polar regions, but it is not so clear whether the form of the convection is small scale (Aurnou *et al.* 2003) or large scale, possibly controlled by the magnetic field (Sreenivasan and Jones 2005). In either case, an azimuthal, or zonal, flow is to be expected. In this article, we use dynamo models to investigate the type of zonal flow associated with the different types of convection. Aurnou *et al.* (2003) considered non-magnetic laboratory convection, and found that although it was in the form of small-scale plumes, it nevertheless drives a substantial anticyclonic zonal flow in the polar regions.

The secular variation of the Earth's magnetic field can be used to evaluate the flow just below the CMB provided some additional hypotheses are added (e.g. Bloxham and Jackson 1991). Although the Oersted and Magsat satellites give accurate information, unfortunately data about the field itself as well as its time-derivative are needed to calculate the core velocities (Eymin and Hulot 2005) and these are uncertain due to lack of knowledge of the crustal components of the geomagnetic field. Nevertheless, all published analyses suggest that there are anticyclonic polar vortices (Olson and Aurnou 1999, Hulot *et al.* 2002). Olson and Aurnou (1999) found a zonal flow with an angular speed of around $0.25^\circ\,\mathrm{yr}^{-1}$.

Since inertial effects are believed not to be important in the slow large-scale components of core flow (Jones 2000, Aubert 2005, Sreenivasan and Jones 2006), the polar azimuthal flow is likely to be a thermal wind u_ϕ, given by

$$2\Omega\frac{\partial u_\phi}{\partial z} = \frac{g\alpha}{r}\frac{\partial T'}{\partial \theta}, \tag{1}$$

if the magnetic wind contribution from the Lorentz force is small. Here Ω is the angular velocity of rotation, g is the acceleration due to gravity and α is the thermal expansion coefficient, θ is the colatitude in spherical polar coordinates, and z is the coordinate parallel to the rotation axis. T' is the temperature fluctuation, i.e. the departure from the adiabatic value. Here $\alpha T' = \delta\rho$ is the density anomaly due to temperature. In the core there will also be a contribution from compositional convection, but here we treat the two effects together. Braginsky and Roberts (1995)

and Starchenko and Jones (2002) noted that the density anomaly could be estimated in terms of the heat flux, F, (which has units $\mathrm{W\,m^{-2}}$)

$$F \sim \rho c_p u_r T'. \tag{2}$$

As we shall see, the zonal flow u_ϕ is typically the same order of magnitude as the radial convective velocity u_r (see also Aubert 2005), so combining (1) and (2) gives the zonal flow

$$u_\phi \sim \frac{d}{R}\left(\frac{g\alpha F}{2\Omega\rho c_p}\right)^{1/2}, \tag{3}$$

where d is the distance from the inner core boundary (ICB) to the CMB, and R is the length scale in the θ-direction, which Aurnou *et al.* (2003) set at $R \sim d/2$. This estimate of the typical core velocity gives similar values to the secular variation estimates; see also Aurnou *et al.* (2003).

There are a number of reasons why the thermal wind might be expected to give rise to anticyclonic flow. If the inner core is gravitationally locked to the mantle (Buffett and Glatzmaier 2000), the assumption we make here, the azimuthal flow is zero near the ICB. If the fluid inside the TC is warmer (less dense) than that outside the TC, then $\partial T'/\partial\theta < 0$ and so u_ϕ becomes more negative as we go outward from the ICB in the northern hemisphere, and negative u_ϕ corresponds to anticyclonic flow. Why should the fluid be less dense inside the TC? Aurnou *et al.* (2003) point out that the flux of compositionally light material and latent heat is released from the ICB inside the TC. If it has difficulty penetrating outside the TC, a build-up of light material inside the polar regions may occur. Another possibility is that the magnetic field makes the convection take the form of a wide plume (Sreenivasan and Jones 2005). Then the fluid inside the rising plume is systematically warmer than the cold descending fluid outside the plume. The Coriolis force then acts to turn the warm rising plume into an anticyclonic vortex. As we see below, it is this second mechanism that dominates most of our models, as the magnetic field usually creates one large dominant plume inside the TC.

In the Earth's atmosphere, the polar regions are of course colder than average due to inhomogeneous solar heating, so the atmospheric polar vortices are cyclonic rather than anticyclonic.

2. Governing equations and parameters

In our dynamo model, a Boussinesq fluid with finite electrical conductivity is confined between two concentric, co-rotating spherical surfaces that correspond to the ICB and the CMB. The radius ratio is fixed at 0.35 corresponding to the Earth's ICB to CMB ratio. The superadiabatic temperatures of the two boundaries are maintained at a constant difference ΔT, driving buoyant convection. Most of the runs are done with no-slip boundary conditions on the ICB and CMB, and with electrically insulating boundary conditions, i.e. no currents in the mantle or the inner core. Some runs were done using stress-free boundary conditions at both ICB and CMB, and a few runs were

done with a finitely conducting inner core. The time-dependent MHD equations for the velocity $\mathbf{u}$, the magnetic field $\mathbf{B}$ and the temperature T are

$$E\mathit{Pm}^{-1}\left(\frac{\partial \mathbf{u}}{\partial t}+(\mathbf{u}\cdot\nabla)\mathbf{u}\right)+2\hat{\mathbf{z}}\times\mathbf{u}=-\nabla p+Ra\frac{\mathbf{r}}{r_o}\,T+(\nabla\times\mathbf{B})\times\mathbf{B}+E\nabla^2\mathbf{u}, \tag{4}$$

$$\frac{\partial \mathbf{B}}{\partial t}=\nabla\times(\mathbf{u}\times\mathbf{B})+\nabla^2\mathbf{B}, \tag{5}$$

$$\frac{\partial T}{\partial t}+(\mathbf{u}\cdot\nabla)T=\mathit{Pm}\,Pr^{-1}\,\nabla^2 T, \tag{6}$$

$$\nabla\cdot\mathbf{u}=0, \qquad \nabla\cdot\mathbf{B}=0. \tag{7, 8}$$

The dimensionless groups in the above equations are the Ekman number, $E=\nu/\Omega d^2$, the Prandtl number $Pr=\nu/\kappa$, the modified Rayleigh number $Ra=g\alpha\Delta T d/\eta\Omega$ and the magnetic Prandtl number, $Pm=\nu/\eta$. The gap-width between the shells is d, ν is the kinematic viscosity, κ is the thermal diffusivity and η is the magnetic diffusivity. The unit of length is $d=2.26\times10^6$ m for the Earth, of time is $d^2/\eta=8.1\times10^4$ years, assuming $\eta=2\,\mathrm{m^2\,s^{-1}}$, and the unit of temperature is ΔT. Taking in the Earth's core $g=8\,\mathrm{ms^{-2}}$, $\alpha=10^{-5}\,\mathrm{K^{-1}}$ and $\Omega=7.3\times10^{-5}\,\mathrm{s^{-1}}$ (Anufriev *et al.* 2005), then $\Delta T=10^{-3}$ K gives a Rayleigh number of 1240. As always in numerical dynamo models, the values of ν and κ are assumed to be enhanced above their true values to ensure numerical stability. Here we assume $Pr=Pm$, which means that the turbulent κ is also $2\,\mathrm{m^2\,s^{-1}}$. Assuming $\rho=10^4\,\mathrm{kg\,m^{-3}}$ and $c_p=860\,\mathrm{J\,kg^{-3}\,K^{-1}}$, the conducted heat flux at the CMB is then $0.35\,\rho c_p\kappa\Delta T/d=2.7\times10^{-3}\,\mathrm{W\,m^{-2}}$, leading to a total conducted heat flux at the CMB of 0.4 TW. Our runs have Ra in the range 500–1750, i.e. up to about 20 times critical. Since the Nusselt number is typically in the range 3–5 for these Rayleigh numbers, our total convective heat flux is in the range 0.3–2 TW, a geophysically reasonable value. Magnetic field is measured in units of $(\rho\Omega\mu\eta)^{\frac{1}{2}}$, ρ being the density and μ the permeability of free space. With our standard Earth-like parameters, the unit of magnetic field is 1.4×10^{-3} T, while a typical value of the observed B_r at the CMB is 5×10^{-4} T. The Ekman number, E is fixed at 10^{-4} in all runs. The code gives close agreement with the dynamo benchmark (Christensen *et al.* 2001) and other dynamo simulations (for example, Christensen *et al.* 1999).

3. Results

3.1. *The effect of inertia on the polar azimuthal flow*

We first study the role played by inertia on the formation of zonal flow inside the TC. If the Rayleigh number is kept constant and the Prandtl numbers Pr and Pm are decreased but kept equal to each other, then the viscosity in the model is reduced and the fluid Reynolds number increases, so the inertial forces become important; see Sreenivasan and Jones (2006) for a full discussion. It is then possible for the

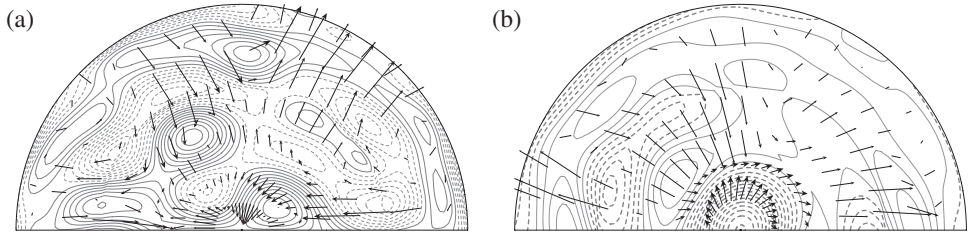

Figure 1. Contour plots of the axial vorticity, ω_z, in the $z = 1.48$ plane, with arrows for the flow perpendicular to z superposed for two cases: (a) $Pr = Pm = 0.2$ and (b) $Pr = Pm = 5$. The Rayleigh number, Ra is fixed at 750 in both cases. The minimum and maximum dimensionless values of the quantities plotted are as follows: (a) $[-5779.3, 6621.8]$, with maximum velocity perpendicular to z (longest arrow) 334.8 and (b) $[-7615.5, 2149.3]$ with maximum velocity perpendicular to z 212.46. Positive values appear in solid lines and negative values in dashed lines. Twofold symmetry in longitude is imposed in these computations.

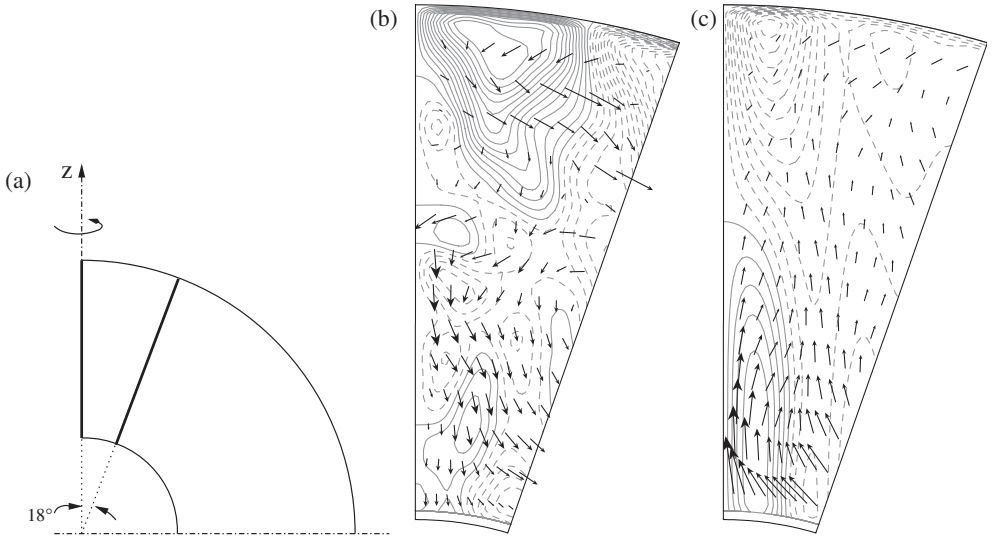

Figure 2. Meridional contours of the azimuthally averaged thermal wind, u_ϕ in a sector magnifying the tangent cylinder region, shown highlighted in (a). The meridional flow arrows are superposed. The parameters are (b) $Pr = Pm = 0.2$ and (c) $Pr = Pm = 5$. In both runs, $Ra = 750$. The minimum and maximum values in the plots are (b) $[-156.7, 128.1]$, with maximum meridional velocity 200.7 and (c) $[-206.9, 79.7]$, with maximum meridional velocity 266.5. Negative values of u_ϕ are shown in dashed lines. Note the change in the direction of u_ϕ.

Reynolds stresses and the meridional circulation to drive a zonal flow which can dominate the thermal wind term. In figure 1(a), we show contour plots in a horizontal section at an elevation $z = 1.48$ above the equatorial plane and lying in the polar region. Note that the plane $z = 1.44$ contains the circle where the tangent cylinder cuts the CMB. We find that the axial vorticity, ω_z, near the polar axis has a positive sign at $Pr = Pm = 0.2$. There is a radial influx of fluid into this zone and from figure 2(b), we see that there is a corresponding downwelling in this region. The meridional plots in figure 2 are azimuthally averaged, with the TC region shown magnified in a sector that makes an angle 18° to the polar axis. Figure 2(a) shows the geometry with the sector highlighted. The azimuthally averaged zonal flow in figure 2(b) is cyclonic (eastward). As $Pr = Pm$ is increased to 5, ω_z becomes negative in a region of upwelling as

seen in figure 1(b), still preserving the negative helicity. The zonal flow is now anticyclonic (see figure 2c), as indicated by the secular variation observations, and is a thermal wind driven by the horizontal temperature gradient as in equation (1). We also note from figure 2(c) that the upwelling column extends from the ICB right into the polar region, drawing fluid inward at its base and expelling fluid radially outward at the top. Hence, there is a weak prograde azimuthal flow near the ICB, the magnitude of which is about one-third of the strong anticyclonic flow at the pole (a weak prograde flow at the ICB is also seen in other simulations; see for example, Glatzmaier and Roberts 1995). We have found that an anticyclonic polar vortex can be realized only for $Pr \geq 0.5$, showing that this is a markedly low-inertia phenomenon, characterized by a magnetic-buoyancy-Coriolis force (MAC) balance. Cyclonic polar vortices are generated when the inertial terms are significant. The magnetic field in such cases is very weak and so the Lorentz forces do not enter the force balance substantially. What ensues is a balance between the buoyancy, inertial and Coriolis forces (Sreenivasan and Jones 2006).

3.2. *The structure of magnetoconvection in the polar regions*

We now focus on low-inertia results at $Pr = Pm = 5$, to understand how the behaviour of these anticyclonic vortices is affected by core convection and the generation of magnetic fields. We have not imposed azimuthal symmetry in the calculations reported henceforth; in other words all azimuthal m-modes up to the truncation value are included in the spherical harmonic expansion. The main noticeable difference between these simulations and those with imposed azimuthal symmetry is that the upwelling that extends from the ICB up to the pole takes place through one or more localized hot spots that are offset from the rotation axis (see figure 3 for one horizontal section of this hot spot, and also Sreenivasan and Jones 2005). The centre of the hot spot lies on a line closely parallel to the rotation axis. If only even parity azimuthal m-modes are included in the simulation (see for example, Christensen *et al*. 1999), the upwelling is forced to lie exactly over the pole as in figures 1 and 2, and the naturally occurring offset found here is missed. This off-axis plume can change its longitudinal position with time, the direction of drift being generally westward (see also Sreenivasan and Jones 2005). At $Ra = 525$, figure 3(a) shows a snapshot of the temperature perturbation T' in which we see three significant hot spots that correspond to the three upwellings in figure 4(a). As the Rayleigh number is increased to 750, there is only one dominant upwelling (see figures 3b and 4b), but the local temperature and axial (z) velocity are higher in that single plume. Also, the size of the plume is larger than that of the individual plumes at $Ra = 525$. The largest single plume occurs near $Ra = 1100$, (figure 3c). However, as the convective driving is made stronger ($Ra = 1450$; see figure 3d), although the strength of the upwelling is greater, its kernel appears to shrink in size. We shall return to this interesting observation in section 4.

We have noted that, at high Ra, the flow within the TC is generally dominated by one or more upwelling plumes. The off-centre plume creating the anticyclonic vorticity is clearly a convective phenomenon as can be seen from the very strong correlation between the temperature and the axial velocity fields shown in figures 3(a), 4(a) and 3(b), 4(b). In figure 4(c), the z-velocity with the magnetic field switched off is given. The Rayleigh number is 750, the same as in figure 4(b), but the convection has an entirely different pattern. The single dominant plume is replaced by a much larger

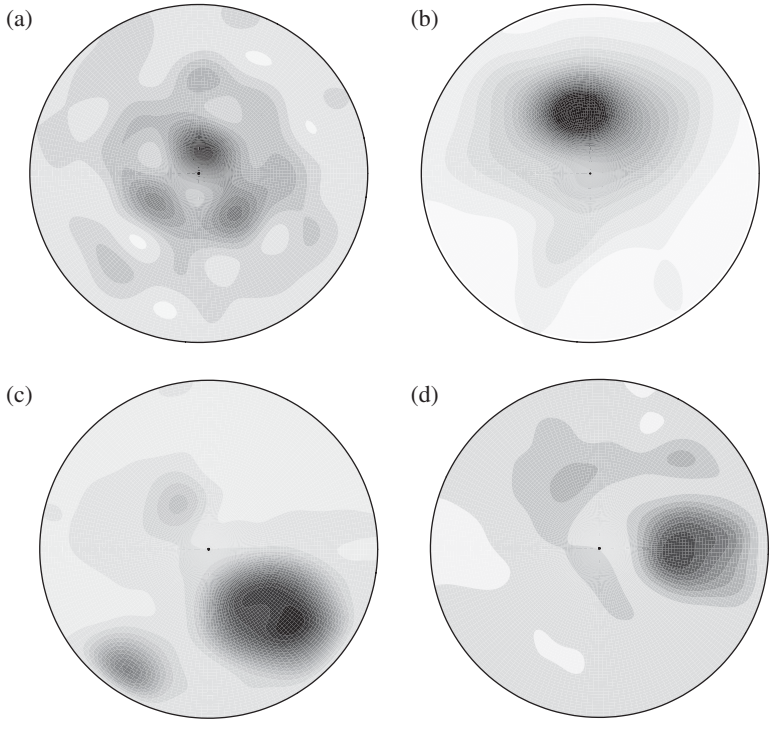

Figure 3. Plots of the temperature perturbation, T' at a section $z = 1.46$ above and parallel to the equatorial plane. The operating parameters are (a) $Ra = 525$, (b) $Ra = 750$, (c) $Ra = 1100$ and (d) $Ra = 1450$. In all runs, $Pr = Pm = 5$. The outer radius of this section in dimensionless units is 0.485 (the tangent cylinder radius is 0.538). No longitudinal symmetry is imposed. The minimum and maximum values in the four figures are as follows: (a) $[-0.002, 0.0192]$ (b) $[-0.003, 0.116]$, (c) $[-0.0037, 0.249]$ and (d) $[-0.009, 0.377]$.

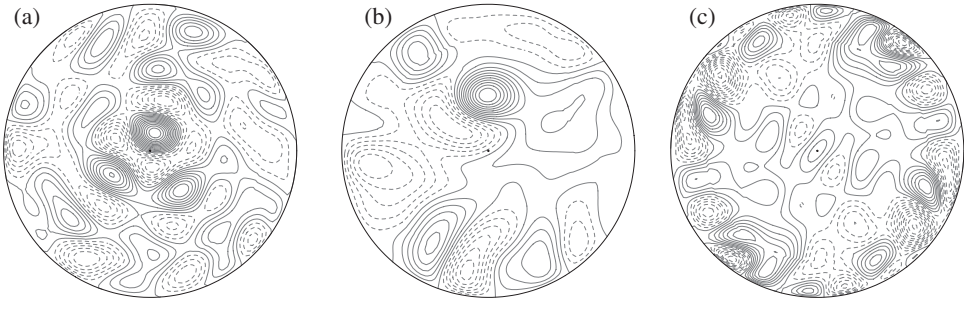

Figure 4. The section $z = 1.46$ above and parallel to the equatorial plane. (a), (b) and (c) give contours of the axial velocity u_z for (a) $Ra = 525$, (b) $Ra = 750$ and (c) $Ra = 750$ with $\mathbf{B} = 0$ imposed. The respective minimum and maximum values for u_z shown are (a) $[-10.01, 17.55]$, (b) $[-24.85, 41.4]$ and (c) $[-5.56, 3.46]$. Positive values of u_z are shown in solid lines and negative values in dashed lines. $Pr = Pm = 5$ in all runs.

number of thinner plumes. Around the edge of the section we see the tops of the convection columns driven by the convection outside the TC, which dominates the rather feeble convection plumes inside. The axial velocity in the absence of the magnetic field is about 10 times weaker than the dynamo run at $Ra = 750$ (compare values for

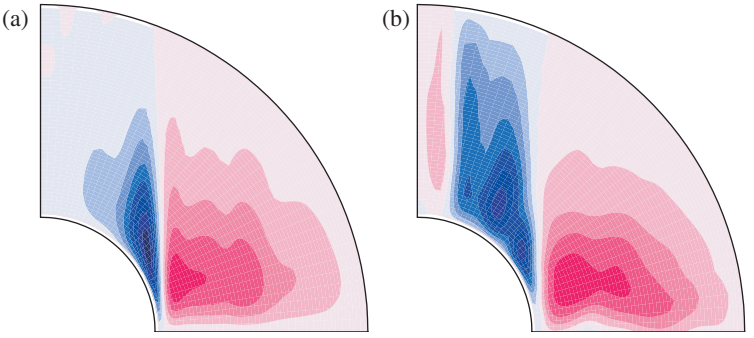

Figure 5. Meridional contour plots of $1/r\,(\partial T'/\partial\theta)$ with (a) pure convection in the spherical shell and (b) dynamo action. Both runs were performed at $Ra = 750$, $Pr = Pm = 5$ and $E = 10^{-4}$. The minimum and maximum values in these figures are: (a) $[-0.86, 0.57]$; (b) $[-0.83, 0.62]$. Note the dominant temperature gradients inside the tangent cylinder (near the polar region) in the presence of dynamo action.

figures 4b and 4c). We also note that the azimuthal wind u_ϕ for pure convection in the spherical shell is much weaker than that in the presence of a dynamo magnetic field at the same parameter values of Ra, Pr and E. In figure 5 we show meridional sections of $1/r\,(\partial T'/\partial\theta)$, which drives the thermal wind by way of equation (1). Note that it is the enhanced horizontal temperature gradient which is responsible for driving the larger zonal flows, not the Lorentz force itself. We therefore conclude that magnetic field has a major effect on the formation of these upwellings.

The upwelling fluid that is channelled through the hot spot is strongly correlated with negative z-vorticity; see figure 6(a–c). The flow field perpendicular to z near the plume is complex as there are not only regions of radial outflow as one would expect in the polar region, but also a localized region of radial inflow which one would not observe when azimuthal symmetry is imposed. The offset of the plume produces this inflow and thereby, the small region of prograde (eastward) azimuthal flow between the vortex and the axis (figures 6e and 6f). The upwelling at $Ra = 525$ is not strong enough to produce a marked prograde patch, but in all higher-Ra runs, the offset of the plume causes this phenomenon. As Ra is increased from 750 to 1450 (i.e. to approximately 20 times the critical value for the onset of non-magnetic convection), the maximum velocity perpendicular to z increases three-fold. The stronger upwelling gives rise to a radially inward flow that is greater than the radially outward flow. Consequently, the prograde azimuthal flow also increases threefold (compare values for figures 6e and 6f). The retrograde (anticyclonic) flow velocity is not significantly affected by the convection for $Ra > 750$ (also see table 1 for the average values of u_ϕ). In short, the only effect of increasing Ra further would be to reduce the transverse dimension of the upwelling plume and create a stronger prograde flow region near the axis.

From the meridional plots of u_ϕ in figure 7, we again see the offset in the upwelling and the presence of the positive (prograde) azimuthal flow closer to the axis. Since the vortex is not axisymmetric, we have chosen a section passing through the centre of a plume to visualize the local flow. Note that the maximum value of u_ϕ in these figures could be 3–4 times the azimuthally averaged maximum values given in table 1. The exception to this is the case with imposed twofold longitudinal symmetry ($m_s = 2$ in table 1) where the azimuthally averaged value of the 'centered' vortex is approximately equal to the local value at any section. The inclination of the vortex to the polar axis,

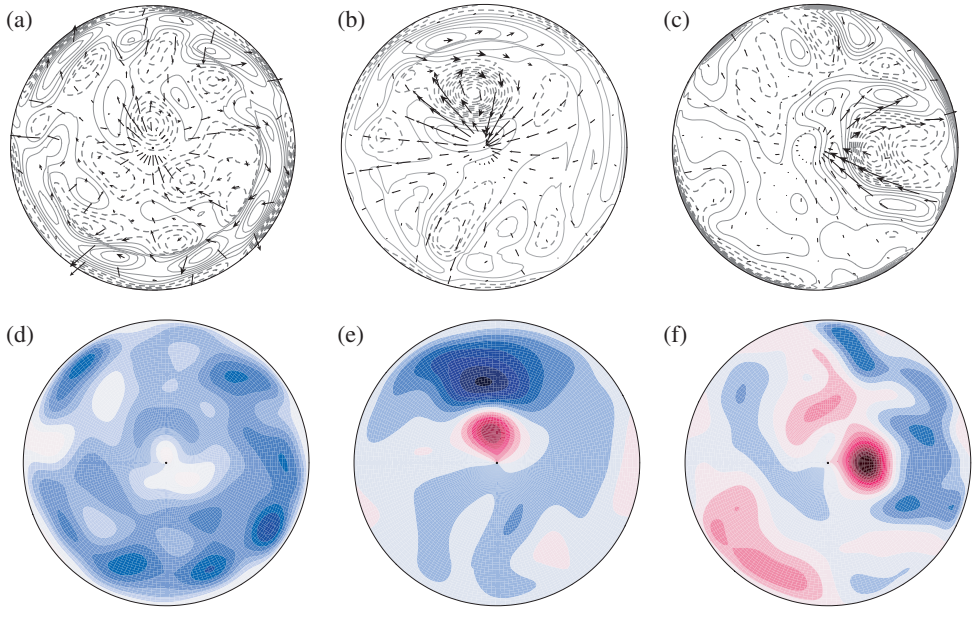

Figure 6. (a), (b) and (c): Contour line plots of the axial vorticity, ω_z with the flow arrows perpendicular to z superposed at the section $z = 1.46$, for the cases (a) $Ra = 525$, (b) $Ra = 750$ and (c) $Ra = 1450$. Negative values are in dashed lines. (d), (e) and (f): Corresponding shaded contours of the azimuthal velocity, u_ϕ at the same section, with positive values in red and negative values in blue. The minimum and maximum values of ω_z are (a) $[-2054.29, 1037.74]$, with maximum velocity perpendicular to z (longest arrow) 67.24, (b) $[-6881.96, 3225.08]$, with maximum velocity perpendicular to z 302.4 and (c) $[-16279, 15248]$, with maximum velocity perpendicular to z 908.79. The minimum and maximum values of u_ϕ are (d) $[-59.9, 8.19]$, (e) $[-239.53, 200.55]$ and (f) $[-276.69, 638.29]$.

Table 1. Summary of the operating parameters in the calculations with electrically insulating boundary conditions. Here, Ra is the Rayleigh number, l is the maximum spherical harmonic degree used, m_s is the azimuthal symmetry imposed (1 for no symmetry), R_m is the magnetic Reynolds number of the dynamo, $\overline{u_\phi}_{max}$ is the maximum ϕ-averaged anticyclonic azimuthal velocity, θ_{pv} is the polar vortex inclination, $B_{r,\mathrm{CMB}}$ is the time-averaged maximum CMB radial magnetic flux obtained, Λ_{max} is the Elsasser number based on the maximum value of B_z and $\bar{\Lambda}$ is the Elsasser number based on the value of $|\mathbf{B}|$ throughout the whole shell.

Figure reference	Ra	l	m_s	R_m	$\overline{u_\phi}_{max}$	θ_{pv}	$B_{r,\mathrm{CMB}}$	Λ_{max}	$\bar{\Lambda}$
1(b), 2(c)	750	48	2	85	206.9	3.7°	1.0	18.4	1.91
3(a), 4(a), 6(a) and (d)	525	48	1	60	33.9	15.3°	0.6	0.92	0.8
3(b), 4(b), 5(b), 6(b) and (e), 7(a), 8(a)	750	56	1	85	71.1	11.6°	1.0	12.0	2.25
3(c), 11(a) and (d)	1100	68	1	115	58.9	10.8°	2.2	64.0	3.80
3(d), 7(b), 8(b), 9(a)–(c)	1450	68	1	150	50.4	11.5°	2.8	104.0	5.10

θ_{pv}, given in table 1 is obtained by measuring the angle made to the axis of rotation by the peak ϕ-averaged u_ϕ from a meridional section. We find that, at large values of Ra (and the magnetic field), θ_{pv} is about 11°, so that at the CMB it occurs around latitude 80°. The diameter of the vortex core is about 15°.

Figure 8 gives the meridional contours of the magnetic field B_ϕ in the TC with arrows giving the length of B_r superposed on them. B_ϕ appears to be mainly created by u_ϕ twisting the z-field component. B_r itself appears to have come mainly from the dipole field

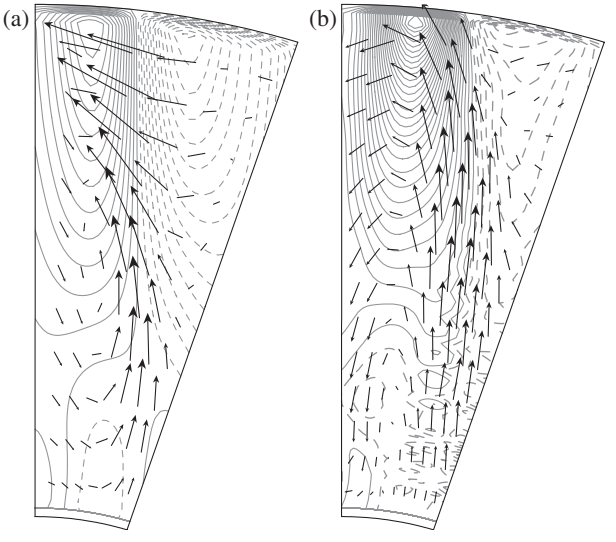

Figure 7. Meridional contour plots of u_ϕ in the section that passes through the centre of the upwelling plume. The meridional flow arrows are superposed. The sector shown has an angle 18°. The line types are as in previous figures. The parameters are (a) $Ra = 750$ and (b) $Ra = 1450$. The minimum and maximum values in these figures are (a) $[-245.4, 207.5]$, with maximum meridional velocity (longest arrow) 106.6; (b) $[-212.2, 750.3]$, with maximum meridional velocity 360.8.

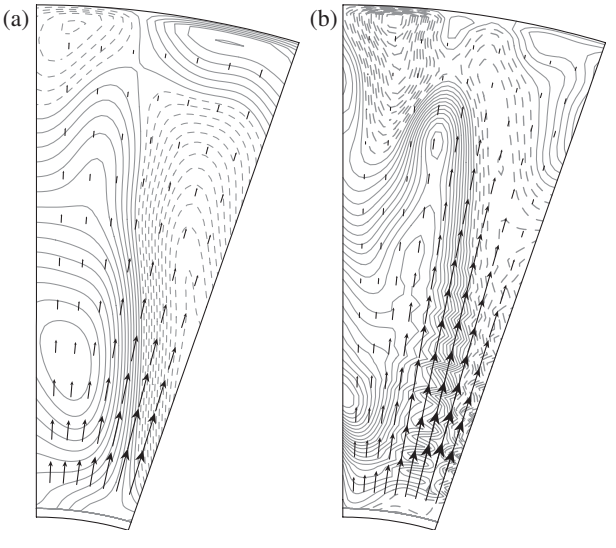

Figure 8. Meridional contour plots of B_ϕ in the section that passes through the centre of the upwelling plume. The arrows depicting B_r are superposed. The sector shown and the parameters are similar to those in figure 7. The minimum and maximum values in these figures are: (a) $[-1.26, 1.37]$, with maximum B_r (longest arrow) 3.462; (b) $[-2.88, 3.77]$, with maximum B_r 10.22.

generated outside the TC diffusing in. Note that B_r is much stronger near the ICB than at the CMB and this is reflected in the large value of the maximum Elsasser number, Λ_{max} in comparison with the volumetric average value, $\bar{\Lambda}$. In section 4, we shall see that Λ_{max} controls the size of the upwelling plumes within the tangent cylinder.

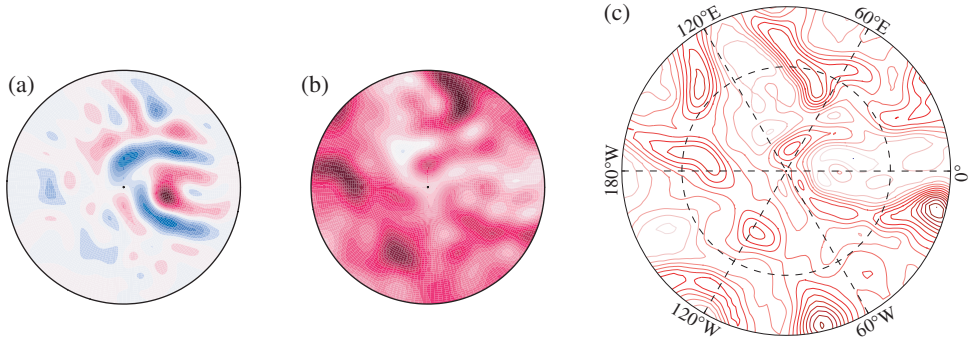

Figure 9. Shaded contour plots of (a) u_r and (b) B_r on the section $z = 1.44$ above the equatorial plane, where the tangent cylinder cuts the outer boundary of the spherical shell. In (c), contours of B_r on a stereographic projection of the polar region between latitude 60°N and the North Pole are shown. The dashed circle gives the location of the tangent cylinder ($\approx 71°$N), to which the outer radius of the section in figure (a) and (b) correspond. The respective maximum and minimum values in the figures are (a) $[-93.7, 183.0]$, (b) $[-0.103, 1.6]$ and (c) $[-0.02, 1.98]$. The Rayleigh number, $Ra = 1450$.

Conversely, the wavenumber perpendicular to z of the observed polar vortex plume could possibly be used to probe the magnetic field that exists near the inner core.

When convection is strong, there is a direct correlation between the flow and the poloidal magnetic field within the TC. From figures 9(a) and 9(b), we find that strong flux patches occur in downwelling regions, and weak or even oppositely signed fields (seen as white) are produced in areas of fluid upwelling. The rising fluid expels magnetic field in its path, thereby creating a field deficit in that region. Conversely, sinking fluid just below the CMB is associated with stronger normal flux patches. However, the correlation is not perfect and a stronger flow does not necessarily result in a stronger or weaker field. The 'whitest' (lowest field) patch in figure 9(b) is not in fact associated with the strongest upwelling vortex, but with a weaker upflow on the other side of the polar axis. In figure 9(c) the contour plot of B_r is shown in stereographic projection. This corresponds to the plot that can be compared with magnetic observations. At $Ra = 1450$, there are some weak reversed flux patches at the CMB associated with the upwelling regions, which are not found at lower Rayleigh numbers. At even higher Rayleigh numbers, one could obtain perceivable reverse flux patches at the CMB associated with the upwelling plumes, but higher Ra requires more resolution than we could achieve numerically.

3.3. *Effect of varying the boundary conditions*

With an inner core whose electrical conductivity is the same as that of the fluid outer core, the polar vortex velocity is generally higher. At $Ra = 750$, the velocity is not significantly greater than that with the insulating core, but at $Ra = 1100$, the strength increases by a factor of two. As seen in figure 10(a), there could be more than one upwelling plume inside the TC at a given instant, but there is one dominant plume that generates the bulk of the anticyclonic azimuthal flow in figure 10(c). From table 2, we note that the conducting inner core generates a higher R_m, and a vortex velocity that could be up to three times bigger than that with an insulating

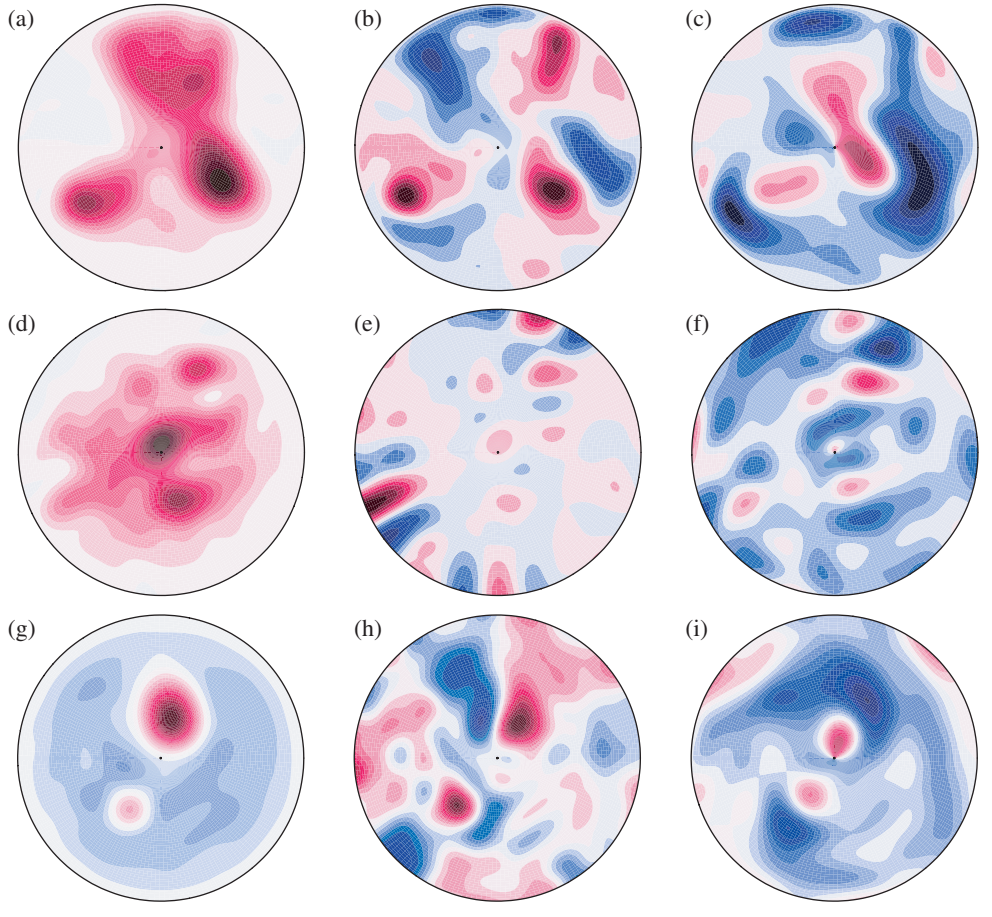

Figure 10. Top row (a), (b) and (c): Coloured contour plots for the case $Ra = 1100$, $Pr = Pm = 5$ with a finitely conducting inner core at the section $z = 1.46$. (a) is the temperature perturbation, T', (b) the axial velocity, u_z and (c) the azimuthal velocity, u_ϕ. Positive values are in red and negative values are shown in blue. The minimum and maximum values are (a) $[-0.014, 0.30]$, (b) $[-130.12, 162.8]$ and (c) $[-500.7, 380.5]$. Middle row (d), (e) and (f): The corresponding contour plots for the case with stress-free, electrically insulating boundaries with the same parameters. The minimum and maximum values are (d) $[-0.001, 0.04]$, (e) $[-78.52, 93.7]$ and (f) $[-253.75, 157.8]$. Bottom row (g), (h) and (i): Plots for the case $Ra = 1750$, $Pr = Pm = 10$, with stress-free, electrically insulating boundaries. The minimum and maximum values are (g) $[-0.068, 0.227]$, (h) $[-88.0, 105.8]$ and (i) $[-748.9, 595.3]$.

Table 2. A comparison of the operating parameters in the calculations with different boundary conditions. No azimuthal symmetry is assumed. R-CIC: rigid, finitely conducting inner core; SF-IIC: stress-free, electrically insulating boundaries (superscripts 1 and 2 denote runs at $Pr = Pm = 5$ and 10); SF-CIC: stress-free, finitely conducting inner core.

Figure reference	BC	Ra	R_m	m_{peak}	$\overline{u_\phi}_{max}$	θ_{pv}	$B_{r,\mathrm{CMB}}$	Λ_{max}	$\bar{\Lambda}$
10(a)–(c)	R-CIC	1100	123.5	6–8	232.23	15.2°	1.4	18.4	4.10
10(d)–(f), 11(b) and (e)	SF-IIC[1]	1100	141	9–11	146.93	3.0°	1.3	1.80	1.55
10(g)–(i), 11(c) and (f)	SF-IIC[2]	1750	219.6	0,9–11	85.0	11.3°	1.2	74.2	1.554
–	SF-CIC	1100	165	9–11	180.0	3.0°	1.4	2.20	1.97

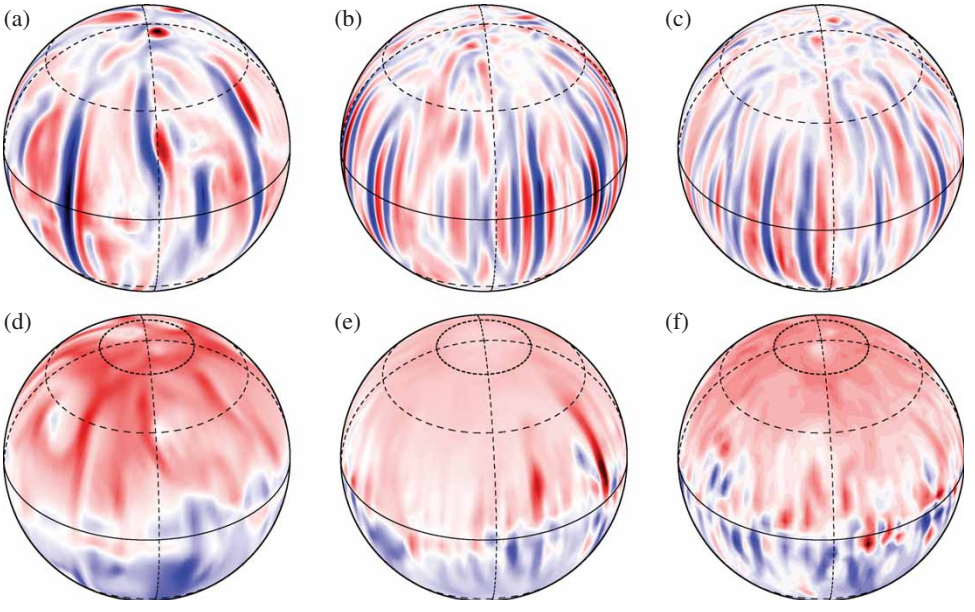

Figure 11. Contour plots of the radial velocity, u_r on the spherical surface $r = 0.8r_o$ and the radial magnetic field at $r = r_o$, for $E = 1 \times 10^{-4}$. The cases shown are (a) and (d) no-slip boundary conditions at ICB and CMB, for $Ra = 1100$, $Pr = Pm = 5$, (b) and (e) stress-free conditions for the same parameters and (c) and (f) stress-free conditions for $Ra = 1750$, $Pr = Pm = 10$. The thick dashed circle in (d)–(f) corresponds to latitude 71°, where the tangent cylinder cuts the spherical surface. The minimum and maximum values are (a) [−324.6, 317.9], (b) [−343.9, 313.5], (c) [−518.1, 398.0], (d) [−1.98, 1.18], (e) [−0.942, 1.29] and (f) [−1.13, 1.21]. Note that the columns are thinner and extend well into the tangent cylinder with stress-free boundary conditions (also see figure 10e). Note that the stress-free case at $Ra = 1100$ has a weaker field inside the TC (latitude 70°).

inner core, though the magnetic field is not necessarily bigger. The peak ϕ-averaged zonal wind is inclined at an angle 15°.

The electrically conducting boundaries certainly affect the solution, enhancing the zonal flow, but there is not a qualitative change in behaviour. Most of the patterns with a conducting core can be seen with insulating boundaries at a slightly different value of the Rayleigh number. With stress-free boundaries, the results for $Ra = 1100$ shown in figures 10(d–f) are significantly different. There is very little convection inside the TC; compare the maximum temperature perturbation values in figure 10(d) and figure 3(c), for example. The strong magnetically controlled vortex is not seen. On the other hand, we find a somewhat larger number of tall, thin convective rolls corresponding to m =9–11 which extend well into the polar region (see figure 11b and compare with the no-slip case figure 11a). However, even though there is very little convection in the polar region (this was also found by Christensen *et al.* 1999), there is nevertheless a substantial anticyclonic vortex. It is more spread out (and axisymmetric) than the magnetically controlled plume vortices, but its total strength can be similar. This vortex probably originates from the polar region being generally warmer than the equatorial regions, perhaps due to the first mechanism (Aurnou *et al.* 2003) mentioned in the introduction. The peak vortex velocity is located quite close to the axis (at about 3° to the z-axis). For non-magnetic convection with stress-free boundaries, the dominant wave mode is $m = 0$ where all the zonal

flow is concentrated and the second dominant mode is in the range $m = 8$–13, corresponding to the number of convection rolls. The polar zonal wind is also approximately 5 times stronger. The role of the dynamo magnetic field is to reduce the magnitude of the polar wind (through Ohmic dissipation) and to concentrate the kinetic energy into the columnar modes.

The lack of convection in the polar regions at moderate values of Ra was considered by Christensen *et al.* (1999) to be responsible for the comparatively weak magnetic field inside the TC in the case of stress-free boundaries. It is also possible that it is the comparatively weak magnetic field in the polar regions that is responsible for reduced convection! In figures 11(d) and 11(e), we show the radial magnetic field on the core mantle boundary for no-slip and stress-free boundary conditions. In the no-slip case there are strong flux patches just outside the TC. These diffuse inward to provide the magnetic field that allows magnetoconvection to occur inside the TC, and hence produce magnetically controlled vortices. Indeed, it is probably the fact that the field is strongest just inside the TC, rather than at the poles, that is responsible for the offset from the polar axis. The plume seeks out the location where the field is strongest. In the stress-free case at $Ra = 1100$, the field is generally somewhat weaker, but it is much weaker near the TC (table 2). In consequence, very little field diffuses inside the TC, and convection is in the form of weak thin plumes. The question of whether the field is weak inside the TC because the convection there is weak, or whether the convection is weak because the field is weak, is rather a chicken and egg situation.

However, if the Rayleigh number is increased in the stress-free case, strong convection is excited within the TC. Isolated upwellings similar to the ones observed at lower Ra with no-slip boundaries appear as in figure 10(g) and (h), which are for $Ra = 1750$. Although there is a big difference between stress-free and no-slip at $Ra = 1100$, the real effect of the stress-free boundaries is just to delay the onset of the magnetic mode of convection to a somewhat higher critical Rayleigh number. When the magnetic mode is established at $Ra = 1750$, the generated polar vortex is non-axisymmetric (compare figure 10i with 10c and 6f, for example). However, at $Pr = Pm = 1$ (not shown in figures), the $m = 0$ mode is dominant in the kinetic energy spectrum. The large-scale zonal flows being generated in the polar region and the excursions of the magnetic field in either hemisphere are reminiscent of a strong presence of inertia in the equation of motion (see Sreenivasan and Jones 2006). For the case $Pr = Pm = 10$, the one presented in this article, we find that inertia has become small enough to restore columnar convection and the dipolar symmetry of the magnetic field; see figures 11(c) and 11(f). Note from table 2 that even when the surface and volumetrically averaged magnetic fields are weak, the maximum B_z (or Λ_{max}) in the spherical shell has increased substantially in the calculation at $Ra = 1750$.

From the above discussion, it is clear that, provided convection is strong enough within the tangent cylinder and inertial effects are negligible in the model, the mechanism of polar vortex generation is practically unaffected by the kinematic and electrical boundary conditions imposed.

4. A plane layer magnetoconvection model

The linear theory of convection in a horizontal plane layer (Chandrasekhar 1961), with the rotation vertical and an imposed vertical magnetic field B_z, provides some insight

despite the curvature of the boundaries in the polar regions. Writing b_z for the perturbation of B_z, j_z for the z-component of the current and ω_z for the z-component of the vorticity, the z-component of curl and curl^2 of the momentum equation, the z-component of the induction equation and its curl, and the temperature equation give

$$E(D^2 - a^2)\omega_z + 2Du_z + \Lambda Dj_z = 0, \tag{9}$$

$$E(D^2 - a^2)^2 u_z - 2D\omega_z + \Lambda(D^2 - a^2)Db_z - a^2\, RaT' = 0, \tag{10}$$

$$(D^2 - a^2)b_z + Du_z = 0, \tag{11}$$

$$(D^2 - a^2)j_z + D\omega_z = 0, \tag{12}$$

$$(D^2 - a^2)T' + u_z = 0, \tag{13}$$

where $D = \mathrm{d}/\mathrm{d}z$ and a is the horizontal wavenumber. Our numerical results suggest that stationary modes are the most relevant modes here, so time-dependence is ignored in this simple model, and we solve the linear stability problem as an eigenvalue problem for Ra and minimize it over a (Chandrasekhar 1961). Λ is an input parameter for this linear problem, but table 1 suggests appropriate values. The results are shown in table 3. The case with stress-free, electrically insulating and constant temperature boundaries,

$$D^2 u_z = u_z = D\omega_z = j_z = T' = 0 \quad \text{on } z = \pm 0.5, \tag{14}$$

uses the formulae given by Chandrasekhar (1961), pages 202, 203, and then converted to our notation. Chandrasekhar noted that there are two modes of convection, the stress-free magnetic mode (denoted by SFM) and the stress-free viscous mode (denoted by SFV). At small E, the viscous mode always has a large wavenumber, scaling like $E^{-1/3}$, corresponding to tall thin convection columns. The magnetic mode

Table 3. Plane layer magnetoconvection results. Critical Rayleigh numbers Ra and corresponding horizontal wavenumbers a are shown. SFM: stress-free magnetic mode; SFV: stress-free viscous mode; NSM: no-slip magnetic mode; NSV: no-slip viscous mode. All results for constant temperature, electrically insulating boundaries with $E = 10^{-4}$. Values for SFV and NSV with $\Lambda \geq 2$ are omitted as the critical Ra for these modes is higher than that of the corresponding magnetic mode.

Λ	0.2	0.335	0.5	1	2	3.45	5	10	50	100
Ra SFM	777.9	472.4	323.1	176.5	114.9	102.6	107.7	147.2	539.9	1042.0
a SFM	3.215	3.202	3.216	3.336	3.744	4.440	5.154	7.059	14.17	17.53
Ra SFV	473.8	472.4	470.8	465.4	–	–	–	–	–	–
a SFV	35.12	34.97	34.77	34.12	–	–	–	–	–	–
Ra NSM	542.8	381.4	280.9	165.7	112.0	101.4	107.0	146.9	541.0	1044.7
a NSM	4.128	3.702	3.556	3.542	3.909	4.615	5.359	7.349	14.62	17.82
Ra NSV	383.9	380.2	375.5	361.4	–	–	–	–	–	–
a NSV	30.99	30.63	30.16	28.45	–	–	–	–	–	–

has $a \approx \pi$ at small Λ, but as Λ increases a also increases, again leading to tall thin magnetically controlled columns. At small Λ, the critical Rayleigh number is least for viscous modes, so they dominate, but at larger Λ the magnetic modes have lower critical Rayleigh number so they take over. At $E = 10^{-4}$ the critical value of Λ at which the changeover occurs is $\Lambda_{cross} = 0.335$, a rather small value. The corresponding results for no-slip boundary conditions,

$$Du_z = u_z = \omega_z = j_z = T' = 0 \quad \text{on } z = \pm 0.5, \tag{15}$$

are listed in table 3 as NSM and NSV for the two types of mode. These were calculated using a Chebyshev polynomial eigensolver; see Roberts and Jones (2000) for details. Changing the boundary conditions does not affect the results much; the main difference is that the viscous modes have slightly higher critical Rayleigh number in the stress-free case (see also Zhang and Jones 1993). This small difference (which reduces in percentage terms as E is reduced) cannot explain why the convection inside the tangent cylinder is so much stronger in the no-slip case than the stress-free case. The difference must be due to the much larger magnetic field occurring in the no-slip case, which, as table 3 shows, dramatically decreases the critical Rayleigh number.

When comparing these table 3 results with our magnetically controlled plumes, we can view the plume as a structure which is approximately axisymmetric about its centre. The radial temperature perturbation dependence is then $T' \sim J_0(a\rho)$, where J_0 is the zero-order Bessel function and ρ is the distance from the plume axis. The first zero of J_0 is $a\rho = 2.405$, so that taking $\Lambda = 100$ from table 1 (see the tabulated value of Λ_{max}) as an appropriate value at $Ra = 1450$, from table 3 we get $a = 17.82$ and so $\rho = 0.13$. This is a measure of the expected plume radius. If we now compare with figure 3(d), remembering that the dimensionless radius of this section is $\sqrt{1.538^2 - 1.46^2} = 0.485$, we see that the dimensionless plume radius is approximately one-third the section radius giving $\rho \approx 0.16$, remarkably close to the predicted 0.13, so this simple model does a surprisingly good job of predicting the plume structure. The plume in figure 3(c) is slightly thicker than that in figure 3(d), but this is what we expect, because the value of Λ is less than 100 at $Ra = 1100$. Again, the simple theory predicts the plume structure correctly. The form of u_z, u_ϕ, ω_z and the horizontal parts of B shown in figures 4, 6, 7 and 8 can also be predicted reasonably well from the linear theory. Since there is also an azimuthal magnetic field component diffusing in from the field generated outside the TC, it might be expected that this would alter the results significantly. However, from figure 5 of Roberts and Jones (2000), which considers the equivalent linear problem with the field horizontal rather than vertical, we see that the same trends occur in this problem too.

We can now explain a number of the features found in our fully nonlinear simulations. The patterns of convection in figure 4(c), where **B** was switched off, is dominated by the viscous modes, and so is the convection in figures 10(d)–(f), the stress-free case where Λ is small. The tendency of the magnetically controlled plumes to be off-axis is also understandable, because in figure 8 we see that the strongest axial field occurs close to the TC, where it has diffused in, and it is weaker directly over the pole. From table 3 we see that minimum critical Ra occurs at $\Lambda \approx 4$ and so the plume seeks out the location where the field has this value, which is not over the pole itself.

An advantage of the simple model is that we can evaluate the behaviour in the limit $E \to 0$, which is not possible in numerical simulations, for reasons of numerical stability. In the stress-free case, Chandrasekhar (1961, pp. 202, 203) shows that the minimum critical Ra occurs when $x = a^2/\pi^2$ satisfies

$$E\pi^2(2x^3 + 3x^2 - 1) = \Lambda + 4\frac{E\pi^2(1+x)^4 - \Lambda(x^2-1)}{\left[E\pi^2(1+x)^2 + \Lambda\right]^2}. \tag{16}$$

The critical Rayleigh number is then

$$Ra = \frac{\pi^2(1+x)\left(\left[E\pi^2(1+x)^2 + \Lambda\right]^2 + 4(1+x)\right)}{x\left[E\pi^2(1+x)^2 + \Lambda\right]}. \tag{17}$$

At small E, the cross-over point at which viscous modes and magnetic modes have the same critical Rayleigh number has $\Lambda = O(E^{1/3})$. The viscous modes have $x = O(E^{-2/3})$, so the dominant balance in (16) is $2E\pi^2x^3 \sim 4/E\pi^2$, giving $a \sim 2^{1/6}\pi^{1/3}E^{-1/3}$ and $Ra \sim 6 \cdot 2^{-1/3}\pi^{4/3}E^{-1/3}$. For the magnetic modes, taking the limit $E \to 0$ in (16) gives $\Lambda^2 \sim 4(x^2-1)$ or $a \sim \pi(1 + \Lambda^2/4)^{1/4}$. Near the cross-over point, magnetic modes have $x \approx 1$, and then $Ra \sim 16\pi^2/\Lambda$. The cross-over point is therefore given by equating the magnetic and viscous critical Rayleigh numbers to get $\Lambda_{cross} \sim 8.2^{1/3}\pi^{2/3}E^{1/3}/3 \approx 7.2E^{1/3}$. This fits well with the results in table 3, which also shows that the no-slip boundary case gives very similar values. As far as the size of the magnetically controlled columns is concerned, $E = 10^{-4}$ is not far off the asymptotic limit. At $\Lambda = 100$ we found a radial wavenumber $a = 17.82$ at $E = 10^{-4}$, whereas for $E \to 0$ the wavenumber is $a = 22.22$, giving a slightly smaller column. The same trend is found for lower Λ, so we may expect the $E \to 0$ columns to be about 25% thinner than our calculations show.

The dynamics of the magnetic mode of convection are not completely straightforward. In steady non-magnetic non-rotating convection, the buoyancy force from hot fluid is directly balanced by the viscous drag on the rising plume. In low E rotating magnetoconvection, the viscous force is negligible. The hot plume drives a thermal and magnetic wind which swirls around the plume axis (equation (10)). This swirl generates a transverse **B** wrapped around the plume from the axial field through the 'omega-effect', and hence an axial current (equation (12)). The Lorentz force then creates a u_z that varies with height through equation (9), allowing the plume to rise. If there is no magnetic field, u_z can only vary with z through the effect of viscosity (small at low E); the no penetration boundary condition then forbids any axial motion, or more exactly only allows an $O(E^{\frac{1}{2}})$ Ekman suction velocity which is also small at low E. An interesting question is the relative importance of the magnetic wind term compared with the thermal wind in equation (10). Since the required swirl can be generated solely by the thermal wind it is not essential for magnetoconvection; the key part of the Lorentz force is the part which overcomes the Proudman–Taylor constraint in equation (9). However, the magnetic wind term is responsible for the narrowing of the convection columns at large Λ. Without the magnetic wind term, the horizontal wavenumber decreases from $a \sim \pi(1 + \Lambda^2/4)^{1/4}$ down to $a \sim \pi$, so without

the magnetic wind we would not see the thinner plumes at larger Ra (compare figures 3(c) and 3(d).

At low Λ the magnetically controlled plume would fill the entire region inside the TC. This is a possible regime for the geodynamo, though a difficult one for simulations. Since the cross-over point is at $\Lambda_{cross} \approx 7.2E^{1/3}$, at the so-called 'turbulent' value of $E \sim 10^{-9}$, where ν and κ have the same value as η, $\Lambda_{cross} \approx 7.2 \times 10^{-3}$. This is less than the observed dipole field at the CMB, so that polar convection is almost certain to be magnetically controlled. However, it is possible that the geomagnetic field lies in the range $7.2 \times 10^{-3} < \Lambda < 1$ where the field is magnetically controlled, but the magnetic wind is small so that the convective plume fills the whole of the polar region inside the TC. In our simulations, Λ_{cross} is higher because of larger E, and so the regime $\Lambda_{cross} < \Lambda < 1$ is only a small region of parameter space.

5. Discussion and conclusions

In Sreenivasan and Jones (2005), the existence of large off-axis thermal plumes in the polar regions which gave rise to anticyclonic vorticity was noted. The westward drift of these patches was also investigated. In this study we investigated the robustness of the large thermal plumes by varying the parameters and boundary conditions in a systematic manner. The thermal plumes have been shown to be related to the magnetic mode of convection, and thus require a minimum field strength in the polar regions. If the field is below threshold, the convection instead takes the form of thin plumes, which nevertheless can give a systematic anticyclonic vortex, as discussed by Aurnou *et al*. (2003).

When applying the results of spherical dynamo simulations to the behaviour inside the core a number of factors must be kept in mind. Since the parameter regime is far from that of the Earth, we must interpret the enhanced diffusion processes we use as arising from small scale turbulence, which we assume to be isotropic. This may not be the case (Braginsky and Meytlis 1990). Also, there is uncertainty about whether stress-free or no-slip boundary conditions are more appropriate in these circumstances, and whether compositional convection (which has zero flux at the CMB) or thermal convection (which has non-zero flux at the CMB) is dominant, and what is the appropriate value of the Rayleigh number. Making different choices could potentially alter the form of core convection significantly. However, a number of fairly robust features have emerged from this study.

(i) Inertial dominance (see the case $Pr = Pm = 0.2$ in figures 1 and 2) gives rise to a cyclonic (eastward) zonal flow. Low inertia is an essential precondition for the generation of an anticyclonic polar vortex. In a simplified case where only even azimuthal modes are retained in the calculations, a strong axisymmetric upwelling flow is generated centered at the polar axis. The thermal wind associated with the hot plume is progressively more anticyclonic as we move upward from the ICB. Consequently, an anticyclonic or 'retrograde' thermal wind is generated at the CMB and a weaker prograde azimuthal flow, as seen in some models is visible at the ICB.

(ii) Convection in the polar regions can take one of two forms, the magnetic mode and the viscous mode. The viscous modes take the form of many tall thin

columns, while the magnetic mode of convection gives a larger coherent structure, usually with one or more dominant plumes. Both forms of convection give rise to an anticyclonic vortex. The magnetic vortex is usually much stronger locally, whereas the non-magnetic vortex obtained from the thin columns seen in figure 4(c) is much weaker and more widespread in an axisymmetric manner. The total axial vorticity averaged over the whole polar cap inside the TC can be similar in both types of convection.

(iii) In computations where no azimuthal symmetry is imposed, a localized 'hot spot' extending from a section near the ICB right up to the polar region, but offset from the polar axis is often formed. From the meridional plot of u_ϕ shown with the tangent cylinder region magnified (figure 7), we find that the plume core is displaced by $\approx 10^\circ$ from the rotation axis, though the plume axis is still fairly parallel to the rotation axis. The hot spots are associated with rising convective plumes and have anticyclonic vorticity near the CMB. These hot spots are the manifestation of the magnetic mode of convection. The radial magnetic field above a hot spot at the CMB is weaker than average, and very strong plumes may even have reversed flux above them.

(iv) The basic properties of the magnetic mode of convection can be modelled by a plane-layer rotating magnetoconvection model (Chandrasekhar 1961). In particular, both this model and the computations show that for the magnetic mode the plume width decreases as the field strength increases, and that the azimuthal flow twists the axial field into an azimuthal field. The plane-layer model has a sharp transition between the viscous mode and the magnetic mode at $\Lambda = 7.2E^{1/3}$. The computations suggest this transition is not quite so sharp in spherical geometry, but all cases where $\Lambda_{max} < 2$ have many thin weak plumes, whereas all runs with $\Lambda_{max} > 10$ are dominated by a single strong plume, though some weaker plumes may also be present. However, with a more strongly supercritical Rayleigh number, convection might be vigorous enough to expel flux from the rising plumes. If this happens, then narrower plunes might occur inside the TC than would be expected from the linear magnetoconvection model.

As mentioned in section 3.2, we noticed that the strong offset plume does not remain at the same longitude, but migrates in a rather irregular fashion, but generally westward. If the large reversed flux patch seen in the north polar region (Olson and Aurnou 1999) is identified with the strongly upwelling magnetic mode of convection found in our simulations, then the drift velocity of the polar reversed flux patch should be identified with the drift velocity of the hot spot. The polar reversed flux patch drifts westward, as do our magnetic mode hot spots, but the drift velocity of 0.25° per year given by Olson and Aurnou is faster than our typical drift velocity. Locally, we do see rotation rates of this order of magnitude about the axis of the upwelling. Thus the vortex seen at $Ra = 1450$ in figures 3(d) and 7(b) rotates anticyclonically about its off-centre axis at about this angular velocity, but because the vortex only occupies a small fraction of the polar region the global rotation rate of the whole polar cap is considerably less than this, and so our hot spots drift more slowly than 0.25° per year. Indeed, the drift speed of our hot spots may be controlled by their interactions with other weaker vortices, as much as by the global flow it induces. We note that the wind speed inside a tornado often exceeds 100 m.p.h., but the drift speed of the whole structure can be

30 m.p.h. or less. Possibly our rather low drift velocity indicates that the Rayleigh number should be increased further. Also we note that a conducting inner core leads to stronger vortices.

With stress-free boundaries, the magnetic mode of convection is excited at high values of Ra, but results with stress-free boundaries are quite different from those with rigid boundaries at moderate values of Ra (750–1100). In rapidly rotating convection, the dissipation of convective modes is generally dominated by the bulk dissipation and not the boundary layers, and there is no great difference in table 3 between the stress-free and no-slip cases. Why then does the magnetic mode of convection not occur with stress-free boundaries at $Ra \sim 1000$? The magnetic mode of convection requires a strong magnetic field inside the tangent cylinder for it to occur, but when it does occur, the strong upward axial flow concentrates any external field and so reinforces the local magnetic field. The slightly lower magnetic field just outside the tangent cylinder in the stress-free case may be insufficient to get this process started, whereas the slightly stronger field generated by the no-slip boundaries is enough to set the magnetic mode plumes off. If this is the case, it may be quite hard to predict when magnetic modes occur, and they may also be subject to hysteresis. Once the concentration of field has occurred, magnetic modes might survive a reduction in Rayleigh number, but to get them to onset from an initial condition with low magnetic field near the TC may require a much higher Rayleigh number. However, by $Ra = 1750$ with $Pr = Pm = 10$ the field outside the TC has become strong enough even with stress-free boundaries for the magnetic mode of convection to occur.

Another issue is the relation of the magnetic mode plumes to the observed radial field on the CMB. This is important because all our observational information about polar vortices is derived from monitoring the secular variation. There does seem to be a strong correlation between upwelling regions and weaker than average B_r, and downwelling regions have stronger than average B_r (compare figure 9a and c). However, our models do not produce the strong reversed field seen in the north polar regions, but only a rather feeble reversed field patch. It is clear that our understanding of polar convection in the core is still far from complete, but getting the observed behaviour of the geomagnetic field near the poles is a powerful constraint on geodynamo models. It is possible that the magnetic mode of convection would produce stronger reversed flux patches at higher Ra, though this is not certain. There does not appear to be much dynamo action inside the TC in our models: the field is mainly generated outside the TC, and then diffuses into the TC where it is massaged by the magnetoconvection. It may be that genuine dynamo action inside the TC is required to produce strong reversed flux patches.

Acknowlegement

This study was sponsored by a research grant from the UK Particle Physics and Astronomy Research Council. The calculations were performed on the UK MHD Clusters based at the University of Exeter and the University of St Andrews.

References

Anufriev, A.P., Jones, C.A. and Soward, A.M., The Boussinesq and anelastic liquid approximations for convection in the Earth's core. *Phys. Earth Planet. Inter.*, 2005, **152**, 163–190.

Aubert, J., Steady zonal flows in spherical shell dynamos. *J. Fluid Mech*., 2005, **542**, 53–67.
Aurnou, J., Andreadis, S., Zhu, L. and Olson, P., Experiments on convection in the Earth's core tangent cylinder. *Earth Planet. Sci. Lett*., 2003, **212**, 119–134.
Bloxham, J. and Jackson, A. Fluid flow near the surface of the Earth's outer core. *Rev. Geophys*., 1991, **29**, 97–120.
Braginsky, S.I. and Meytlis, V.P. Local turbulence in the Earth's core. *Geophys. Astrophys. Fluid Dynam*., 1990, **55**, 71–87.
Braginsky, S.I. and Roberts, P.H., Equations governing convection in the Earth's core and the geodynamo. *Geophys. Astrophys. Fluid Dynam*., 1995, **79**, 1–97.
Buffett, B.A. and Glatzmaier, G.A., Gravitational braking of inner-core rotation in geodynamo simulations. *Geophys. Res. Lett*., 2000, **27**, 3125–3128.
Busse, F.H., Thermal instabilities in rapidly rotating systems. *J. Fluid Mech*., 1970, **44**, 441–460.
Chandrasekhar, S. *Hydrodynamic and Hydromagnetic Stability*, 1961 (Clarendon Press: Oxford).
Christensen, U., Olson, P. and Glatzmaier, G.A., Numerical modelling of the geodynamo: a systematic parameter study. *Geophys. J. Int*. 1999, **138**, 393–409.
Christensen, U.R. and 15 others, A numerical dynamo benchmark. *Phys. Earth Planet. Inter*., 2001, **128**, 25–34.
Eymin, C. and Hulot, G., On core surface flows inferred from satellite magnetic data. *Phys. Earth Planet. Inter*., 2005, **152**, 200–220.
Glatzmaier, G.A. and Roberts, P.H., A three-dimensional convective dynamo solution with rotating and finitely conducting inner core and mantle. *Phys. Earth Planet Inter*. 1995, **91**, 63–75.
Hulot, G., Eymin, C., Langlais, B., Mandea, M. and Olsen, N., Small-scale structure of the geodynamo inferred from Oersted and Magsat satellite data. *Nature*, 2002, **416**, 620–623.
Jones, C.A. Convection driven geodynamo models. *Phil. Trans. R. Soc. Lond*., 2000, **358**, 873–897.
Jones, C.A., Mussa, A.I. and Worland, S.J., Magnetoconvection in a rapidly rotating sphere: the weak-field case. *Proc. R. Soc. Lond. A*, 2003, **459**, 773–797.
Kageyama, A. and Sato, T., Velocity and magnetic field structures in a magnetohydrodynamic dynamo. *Phys. Plasmas*, 1997, **4**, 1569–1574.
Olson, P. and Aurnou, J., A polar vortex in the Earth's core. *Nature*, 1999, **402**, 170–173.
Roberts, P.H. and Jones, C.A., The onset of magnetoconvection at large Prandtl number in a rotating layer. I. Finite magnetic diffusion. *Geophys. Astrophys. Fluid Dynam*., 2000, **92**, 289–325.
Sreenivasan, B. and Jones, C.A., Structure and dynamics of the polar vortex in the Earth's core. *Geophys. Res. Lett*., 2005, **32**, L20301.
Sreenivasan, B. and Jones, C.A., The role of inertia in the evolution of spherical dynamos. *Geophys. J. Int*., 2006, **164**, 467–476.
Starchenko, S. and Jones, C.A., Typical velocities and magnetic field strengths in planetary interiors. *Icarus*, 2002, **157**, 426–435.
Zhang, K. and Jones, C.A., The influence of Ekman boundary layers on rotating convection. *Geophys. Astrophys. Fluid Dynam*., 1993, **71**, 145–163.